EXHIBIT 25

NIH Public Access
Author Manuscript

On locating the obstruction in the upper airway via numerical simulation

Yong Wang and **S. Elghobashi**[*]
Department of Mechanical & Aerospace Engineering, University of California, Irvine, CA 92697, USA

Abstract

The fluid dynamical properties of the air flow in the upper airway (UA) are not fully understood at present due to the three-dimensional (3D) patient-specific complex geometry of the airway, flow transition from laminar to turbulent and flow-structure interaction during the breathing cycle. It is quite difficult at present to experimentally measure the instantaneous velocity and pressure at specific points in the human airway. On the other hand, direct numerical simulation (DNS) can predict all the flow properties and resolve all its relevant length- and time-scales. We developed a DNS solver with the state-of-the-art lattice Boltzmann method (LBM), and used it to investigate the flow in two patient-specific UAs reconstructed from CT scan data. Inspiration and expiration flows through these two airways are studied. The time-averaged first spatial derivative of pressure (pressure gradient), $\partial p/\partial z$, is used to locate the region of the UA obstruction. But the time-averaged second spatial derivative, $\partial^2 p/\partial z^2$, is used to pinpoint the exact location of the obstruction. The present results show that the DNS-LBM solver can be used to obtain accurate flow details in the UA and is a powerful tool to locate its obstruction.

Keywords

1. Introduction

The human upper airway, UA, includes the parts of the respiratory tract above the thorax, i.e. the nasal cavity, the pharynx, the larynx and the upper part of the trachea. Common surgeries for correcting the UA obstruction include septoplasty, tonsillectomy and adenoidectomy. In the United States, about 600,000 children undergo adenotonsillectomy operation each year. However, the success rate of these operations is only about 50% due to

[*]Corresponding author. Tel.: +1 949 824 6131; fax: +1 949 824 8585. selghoba@uci.edu (S. Elghobashi).

Conflict of interest statement
To the best of our knowledge there is no conflict of interest.

Wang and Elghobashi   Page 2

lack of information on where the flow is constricted and where the UA dynamically collapses. Thus, understanding the UA flow properties and accurately locating the obstruction are of practical importance.

Several experimental studies have been carried out to measure the flow properties in laboratory models of the airway. However, the lack of complete fidelity of hot-wire and particle image velocimetry has been demonstrated by Johnstone et al. (2004) and Pollard et al. (2012). On the other hand, computational fluid dynamics (CFD) methods have become increasingly capable of simulating the biofluid flows (Yoganathan et al., 2004; Kleinstreuer and Zhang, 2010; Calay et al., 2002; Doorly et al., 2008; Wen et al., 2008; Choi et al., 2009; Zhu et al., 2011; Na et al., 2012; Deng et al., 2013; Gambaruto et al., 2012; Xi et al., 2012), and providing quantitative information about the flow properties that can minimize the guess work in corrective surgeries.

The flow in the UA is 3D, time-dependent, undergoes transition from laminar to turbulent, and reverses its main direction about every two seconds. The complex geometry of the UA results in curved streamlines, recirculation regions, secondary and jet flows. For example, the minimum cross-sectional area in the overlap region between the nasopharynx and oropharynx usually generates a turbulent jet downstream of the restriction in the apnea cases. Therefore, in order to predict this flow accurately, the numerical method should be able to simulate low Reynolds number turbulent flow in complex geometry efficiently and with minimum empiricism.

In order to investigate the laminar-transitional-turbulent flow in the airway, three approaches with different accuracies have been adopted in the literature: the Reynolds-Averaged Navier-Stokes (RANS), Large Eddy Simulation (LES) and Direct Numerical Simulation (DNS). In RANS approach, Reynolds-averaged Navier-Stokes (NS) equation generates a number of statistical correlations between all the dependent variables and thus creates more unknowns than the available equations, leading to the closure problem. The closure is achieved via mathematical models (such as $k - \omega$ and $k - \varepsilon$) with additional transport equations that usually require fine-tuning for different turbulent flows. Although the accuracy of RANS is acceptable in simple turbulent flows such as straight pipes and channels, it is questionable in turbulent flows with strong streamline curvature, flows in transition from laminar to turbulent and low Reynolds number turbulent flows. All these challenging flows exist in the UA. LES is more accurate than RANS, as large scale turbulent structures (eddies) are numerically resolved and only small (sub-grid scale) structures are modeled by methods similar to RANS. However, LES is not as accurate as DNS due to the empiricism of sub-grid scale models. In DNS, all relevant length- and time- scales are resolved numerically. Thus DNS produces the most accurate information about turbulent flows and is the gold standard for evaluating the accuracy of other methods.

Mihaescu et al. (2008) used both RANS and LES to simulate the flow in a pharyngeal airway model. Large differences were observed between the RANS and LES results of the axial velocity downstream of the maximum narrowing. The authors stated that RANS is not suitable for the UA whereas LES is. Mylavarapu et al. (2009) performed both simulations and experiments for a human UA. The RANS with two-equation turbulence models ($k - \varepsilon$, k

$- \omega$, and $k - \omega$–Shear Stress Transport (SST)) as well as one-equation Spalart-Allmaras model, and LES were used. Mylavarapu et al. stated that the $k - \varepsilon$ model resulted in the best agreement with the experimental data. Zhang and Kleinstreuer (2011) performed simulations for an idealized UA laboratory model with RANS and LES. They found that the RANS with SST transition model produced a better prediction of the turbulence kinetic energy profiles in some cases, while the $k - \omega$ model amplified the flow instabilities after the constriction, and suggested that more accurate turbulence models are still needed for the turbulence-onset prediction in complex geometries. It is clear from the above review that neither RANS nor LES is capable of accurately predicting the flow in the human UA.

The conventional approach for DNS is DNS-NS which solves the three-dimensional Navier-Stokes equations numerically in simple geometries at moderate Reynolds numbers. However, in complex geometries such as that of UA, it becomes computationally prohibitive for DNS-NS to resolve the flow in the near-wall regions. Lin and Tawhai (2007) employed DNS with second-order characteristic Galerkin fractional four-step finite element method to simulate the airflow in human intra-thoracic airways, and concluded that the simulation should consider both the UA and the intra-thoracic airway. An alternative DNS approach is the DNS-LBM which solves the discretized lattice Boltzmann equations (Succi, 2001; Sukop and Thorne, 2005) and is well-suited for resolving all the relevant length- and time-scales of flows confined by walls with complex geometries which are typical of the UA. Compared to the conventional DNS-NS, DNS-LBM has several advantages as will be discussed at the end of Section 2.1.

LBM has been introduced twenty years ago and developed rapidly in the past ten years. It has been used in simulating biomedical flows, such as flows in the respiratory system (Ball et al., 2008; Finck et al., 2007; Hörschler et al., 2010; Eitel et al., 2010; Lintermann et al., 2012) and cardiovascular system (Munn and Dupin, 2008; Boyd and Buick, 2008; Kim et al., 2010). The published LBM studies related to the UA are mostly concerned with the laminar flow in the nasal cavity (Finck et al., 2007; Eitel et al., 2010). These studies demonstrated the capability of the LBM for predicting the complex flow in the UA. Recently, the DNS-LBM has been used to simulate the laminar-transitional-turbulent flows in an idealized laboratory model of the airway (Ball et al., 2008). The results of Ball et al. showed that the DNS-LBM was superior to RANS as it reproduced the critical flow features observed in the experiment. Some other DNS-LBM studies for the flows in patient-specific nasal cavities can be found in Hörschler et al. (2010) and Lintermann et al. (2012).

The objective of the present study is to numerically investigate the flow in real UA (including the nasal cavity, pharynx, larynx and trachea) via DNS-LBM, and develop a method for locating the obstruction based on the fluid dynamic properties of the flow. The DNS-LBM is described in Section 2. Validation of the DNS-LBM is discussed in Section 3. The computational details are described in Section 4. Results of the UA simulations and discussion are presented in Section 5. The proposed method for locating the obstruction is discussed in Section 6. The conclusions are summarized in Section 7.

Wang and Elghobashi

2. Numerical method

2.1. Lattice Boltzmann method

In order to understand the complex flow in the human UA and produce accurate flow properties for pre-surgery decisions and virtual surgery, the state-of-the-art LBM is selected as the DNS method. We developed a 3D solver based on the standard LBM with stream-collision procedures (Succi, 2001; Sukop and Thorne, 2005). Our DNS-LBM solver uses massively-parallel computers efficiently due to the natural parallel characteristics of the LBM.

Both single-relaxation time, SRT (also known as BGK) (Qian et al., 1992), and multi-relaxation time (MRT) (d'Humières et al., 2002) collision operators are considered in our DNS-LBM solver. In the LBM with BGK collision operator, the fluid particle probability density distribution function f_α obeys a set of lattice BGK equations:

$$f_\alpha(\boldsymbol{x}+\boldsymbol{c}_\alpha\delta t, t+\delta t)-f_\alpha(\boldsymbol{x},t)=\frac{f_\alpha^{\text{eq}}(\boldsymbol{x},t)-f_\alpha(\boldsymbol{x},t)}{\tau}, \quad (1)$$

where $\boldsymbol{x}$ is the spatial coordinate of fluid particle; δx and δt are the lattice spacing and time increment respectively; f^{eq} is the local equilibrium distribution function; $\tau = \tau'/\delta t$ is the non-dimensional relaxation time, which is a function of the kinematic viscosity ν, δt and sound speed c_s according to $\nu=c_\text{s}^2(\tau-0.5)\delta t$; α is the directional index of the discrete velocity vector $\boldsymbol{c}_\alpha$. The arrangement of $\boldsymbol{c}_\alpha$ in the velocity space is called lattice. One of the most popular lattices for 3D flow is the D3Q19 lattice which we used in our simulations.

The left-hand side of Eq. (1) represents the streaming motion of the fluid particles, whereas the right-hand side describes their collision. The macroscopic fluid density ρ and velocity $\boldsymbol{u}$ are functions of f_α, while the pressure is calculated from $p=c_\text{s}^2\rho$. It should be noted that the incompressible Navier-Stokes equations can be obtained from Eq. (1) using Chapman-Enskog expansion (Succi, 2001). In our simulation, the 3D computational domain is divided into a number of uniform 3D cells which coincide with the lattice if $\delta x = \delta t = c$. The node at the center of each lattice is connected to the neighboring by the velocity vectors $\boldsymbol{c}_\alpha$.

When the MRT collision operator is used instead of the BGK operator, the relaxation coefficient $1/\tau$ on the right-hand side of Eq. (1) is replaced by a collision matrix $\Lambda_{\alpha\beta}$

$$f_\alpha(\boldsymbol{x}+\boldsymbol{c}_\alpha\delta t, t+\delta t)-f_\alpha(\boldsymbol{x},t)=\Lambda_{\alpha\beta}(f_\beta^{\text{eq}}(\boldsymbol{x},t)-f_\beta(\boldsymbol{x},t)), \quad (2)$$

where $\Lambda_{\alpha\beta} = \boldsymbol{M}^{-1}\,\boldsymbol{SM}$; $\boldsymbol{M}$ is a given $m \times m$ transformation matrix for the DnQm lattice; $\boldsymbol{S} = \text{diag}(s_1, s_2, \ldots, s_m)$ and s_α can be determined by linear analysis and some physical parameters such as viscosity (d'Humières et al., 2002). The MRT operator allows the solution of Eq. (2) to be more stable than that of Eq. (1), at the cost of slightly more computational time. It is noted that most of the published LBM studies on the respiratory system used the BGK operator (Finck et al., 2007; Hörschler et al., 2010; Eitel et al., 2010; Lintermann et al., 2012).

It is clear that the linear LBM Eqs. (1) and (2) are simpler than the nonlinear NS equations and are readily parallelizable. Moreover, the pressure is a local property in the DNS-LBM, whereas in DNS-NS the pressure is obtained by solving the elliptic Poisson equation at a considerable computer cost. Thus the DNS-LBM is certainly more computationally efficient than the conventional DNS-NS methods.

2.2. Boundary Conditions

In the DNS-LBM, only the mesoscopic distribution functions, f_a, need to be prescribed at the boundaries. An extrapolation method (Guo et al., 2002) is adopted to treat straight or curved boundaries in the DNS-LBM solver. In this method, the distribution functions f_a are prescribed at the nodes adjacent to the boundary if that boundary intersects the planes connecting the lattice nodes. In particular, the distribution functions are decomposed into equilibrium and nonequilibrium parts. Fluid properties such as density, pressure and velocity at the external (not in the flow domain) nodes are determined through extrapolation of those at the neighbouring fluid nodes and the physical boundary condition. The equilibrium parts of f_a are then calculated based on these properties. The nonequilibrium parts of f_a are approximated using an extrapolation based on the nonequilibrium parts at the neighbouring fluid nodes. Numerical tests show that such extrapolation method is of second order accuracy (Guo et al., 2002).

3. Solver validation

We have validated our DNS-LBM solver with both BGK and MRT collision operators by performing several simulations of canonical flows. Two-dimensional laminar Poiseuille flow and Taylor-Green vortex flow were computed via the DNS-LBM and produced excellent agreement with the analytical solutions. Three-dimensional laminar curved pipe flow with $Re = 484$ and Dean number $De = 183$ was simulated and the streamwise velocity profiles at $l/a = 19.54$ agree with the experimental data of Humphrey et al. (1985), as shown in Fig. 1. l and a are respectively the distance from the pipe entry measured along the circular path through the pipe center and the radius of the pipe.

Fig. 2 shows a comparison between our DNS-LBM with BGK operator and the DNS-NS results of Kim et al. (1987) for the 3D turbulent channel flow with $Re_\tau = 180$. Our DNS-LBM predictions of the mean velocity and stresses profiles agree well with those of DNS-NS of Kim et al. (1987). Small discrepancies between the DNS-LBM and DNS-NS results near the channel center ($y^+ > 100$) are due to the smaller extent of our computational domain in the spanwise direction, as has already been stated by Bespalko et al. (2009).

We have also computed the flow in the idealized UA laboratory model of Ball et al. (2008) with both BGK and MRT collision operators. For the case with $Re = 677$ at the inlet plane, the instantaneous velocity contours in the central plane and several cross planes are shown in Fig. 3(a). The computed instantaneous vorticity contours in a cross section in the oropharynx are shown in Fig. 3(b). They agree with the experimental image from smoke array visualization.

4. UA simulation details

The present study considers two patient-specific UAs shown in Fig. 4. They were reconstructed from CT scan data by our medical collaborators. The UA in Fig. 4(a) is for a 8-year-old child without respiratory disease, labeled as normal. Fig. 4(b) is for a 7-year-old child with adenotonsillar hypertrophy (airway obstruction is in the oropharynx). The UA in Fig. 4(b) is labeled as obstructed. It can be seen that the geometry of the human UAs is much more complex than that of the idealized model in Ball et al. (2008).

During the CT scans, the gantry tilt was zero in both the normal and obstructed cases. The CT scan parameters are presented in Table 1. The resolution is given as X by Y in the axial plane (e.g., 0.438×0.438), then by axial increment (e.g., the axial increment was 0.3 mm for the normal case). Segmentations were based on an initial selection of pixels whose Hounsfield units ranged between -1024 and -350 (water = 0), with hand edits to eliminate artifacts due to locally poor anatomical resolution.

Both inspiration and expiration phases of the breathing cycle were considered for the normal and obstructed UAs. The walls of the UAs were assumed smooth and rigid, and the two-way interactions between the air flow and walls were not accounted for. The no-slip condition was imposed at the walls. Constant flow rates with uniform velocity profiles perpendicular to the inlet planes were prescribed at the inflow boundary. A pressure boundary condition, where the static pressure is assumed to be a constant value p_0, was applied at the outlet planes. During inspiration, the inlet and outlet planes were located at the nostrils and trachea respectively. During expiration, the inlet and outlet planes exchanged their locations.

It should be noted that the pressure difference between the inlet and outlet planes during breathing is small (about 300Pa = 0.3%p_0, where p_0 is the reference pressure assumed equal to 1 atm). In the LBM, the pressure and density are related via $p = c_s^2 \rho$. In other words, a 0.3% difference in the pressure between the inlet and outlet planes means 0.3% difference in the density at these planes. Both BGK and MRT collision operators were tested. With the BGK collision operator, the smaller τ (or smaller δt), the more accurate the result. However, the solution becomes unstable when τ approaches 0.5. In order to avoid this numerical instability, we used the MRT collision operator in the simulations of the human UAs.

The computations were performed on BlueWaters (BW), a Cray XE6/XK7 supercomputer. The flow parameters and computational details are given in Table 2. A range of flow rates (2–50 L/min) was considered in simulations. The turbulent flow cases with two flow rates (25 L/min for the normal UA and 15 L/min for the obstructed UA) were studied in detail and are presented here. The flow rate for the obstructed airway is smaller than that of the normal airway due to the smaller cross sectional area of the inlet planes in the former and the existence of the obstruction. A uniform Cartesian grid was used. The mesh size (number of lattices), mesh resolution (lattice spacing), δx, and time increment, δt, were selected according to the results of mesh- and time increment- independence tests. Table 2 shows that a finer mesh and smaller time increment were used for the normal UA since its flow rate was larger than that of the obstructed UA. Processor times include the simulation and files output times.

5. Results and discussion

5.1. Flow fields during inspiration

During inspiration, air flows from the nostrils to the trachea. Due to the sudden expansion of the airways after the nostrils, recirculation zones persist in the superior area of the nasal cavity. The velocity contours at eight cross sections are presented in Fig. 5 (a). Sections N1–N8 in the normal UA and O1–O8 in the obstructed UA represent the nasal valve, anterior turbinates, middle turbinates, pharynx, base of tongue, tip of epiglottis, middle of epiglottis and glottis, respectively. Although the inlet velocity (3 m/s) of the normal UA is larger than that (2 m/s) of the obstructed one, the max velocity in the normal UA is 7.34 m/s which is slightly smaller than 7.97 m/s in the obstructed UA. This is due to the existence of the obstruction in the latter.

Fig. 5 (b) displays the temporal variations of two instantaneous velocity components (u_y and u_z) at typical points in the eight cross sections. It should be noted that the negative instantaneous values of u_z are because the downward flow during inspiration is in the opposite direction to the positive coordinate z. In the normal UA, the velocity at the point in cross section N1 is nearly constant. This is because the prescribed boundary condition at the nostrils is that of uniform and constant velocity and the flow is laminar in the nasal valve. The flow is then divided into several streams through the multiple channels of the turbinates. The velocity is almost sinusoidal at cross section N2 and then fluctuates irregularly at N3, indicating a transition from laminar to turbulent flow. After the nasal cavity, the air passes through the pharynx (N4). The flow at section N4 is already turbulent. In the obstructed UA, the velocities u_y at sections O1–O3 are steady but increase monotonically in the main flow direction, indicating the flow is still laminar in the nasal cavity of the obstructed UA. However, after passing through O4, the flow becomes turbulent. This is because the reduced cross-sectional area in the region between the nasopharynx and oropharynx generates a jet downstream of the restriction. It should be noted that most of the cited relevant references considered only the nasal cavity flows. It is shown here that the flow in the pharynx, larynx and trachea is turbulent and unsteady. The contours of vorticity components in the main flow directions at these cross sections are also calculated but not shown. Vortices can be found at sections N4–N8 in the normal UA and O4–O8 in the obstructed UA, indicating secondary streams at these cross sections.

Fig. 6 shows the instantaneous velocity contours in the sagittal plane of both UAs during inspiration. The exact locations of these planes are shown in Fig. 9. The flows near the epiglottis are turbulent in both UAs as evident by the velocity fluctuations in Fig. 5 (b) at sections N6–N7 and O6–O7. A jet flow is seen in Fig. 6 (b) in the region close to the epiglottis.

5.2. Flow fields during expiration

During expiration, air flows from the trachea to the nostrils. The velocity contours at the eight cross sections and velocity components at typical points in these sections are presented in Fig. 7. It can be seen that the flow is laminar in the trachea (N8 and O8) in both UAs. The flow is then accelerated as it passes through the epiglottis, and becomes turbulent in the

pharynx (N5 and O5). Jet flows start near the tip of the epiglottis in both the normal and obstructed UAs, as shown in Fig. 8.

6. Locating the obstruction

6.1. Previous experimental approaches

There are currently two experimental approaches for locating the airway collapse in obstructive sleep apnea using pressure sensors (Han et al., 2002). The first approach assumes that the pressure-time $(p - t)$ fluctuations disappear upstream of the obstruction during apnea since there is no airflow (Hudgel, 1986; Katsantonis et al., 1993; Han et al., 2002). The second approach locates the obstruction using the pressure differences between the sensors (Skatvedt, 1995) since a large pressure difference would occur before and after a flow constriction.

In order to verify the above two approaches, we obtained from our DNS-LBM results the $p - t$ signals at seven points (A–G) in the normal and obstructed airways during inspiration and expiration, and present in Fig. 9. In the normal UA, in Fig. 9 (a), the amplitudes and frequencies of pressure fluctuations at points A and B are nearly the same (with a slight phase shift) during inspiration as they are both located at the end of the nasal passages. The figure shows that the maximum pressure drop is between points C (green) and D (blue) indicating that the maximum resistance to the flow is between the nasopharynx and the oropharynx during inspiration in this normal UA. During expiration, the maximum pressure is at point G as the airflow changes direction.

Figure 9 (b) shows the $p - t$ signals in the obstructed airway. Since the obstructed UA is not totally constricted in our simulation, the pressure fluctuations do not disappear, but their amplitudes and frequencies are reduced as compared to those in the normal UA. It should be noted that the inlet flow rate for the normal UA was 25 L/min whereas that for the obstructed UA was 15 L/min as mentioned earlier. However, it is not possible to determine the location of the obstruction unambiguously from the $p - t$ signals of Fig. 9.

6.2. A new method for locating the obstruction

Since it is not possible to locate the UA obstruction from the $p - t$ signals, we propose a method for locating the obstruction based on the local distribution of the first and second spatial derivatives of pressure. In order to introduce this method, we consider a steady laminar flow in a 2D channel containing an obstruction marked by the letters bcd in the sketch shown in Fig. 10. The flow is from left to right in the positive z direction. The pressure decreases from a to c and reaches a minimum at the narrowest cross section c where the flow attains its maximum velocity (due to continuity). As the flow area increases from c to d, the velocity decreases and the pressure increases. The pressure increase from c to d usually creates a recirculation zone (flow reversal) due to the adverse pressure gradient. Figure 10 (b) shows the variation of the corresponding first derivative of pressure along the channel. The first derivative $\partial p/\partial z$ is negative in the zones a–b and b–c, positive in the zone c–d, and negative again in d–e. The maximum change in $\partial p/\partial z$ occurs in the zone b–d, and results in $\partial^2 p/\partial z^2$ having its maximum positive value at the narrowest section c. Thus, we can use our DNS results to find the location of the maximum change in the first derivative of

Wang and Elghobashi   Page 9

pressure and positive second derivative along the flow direction in the UA, and that will be where the obstruction is.

6.3. Verification for the proposed method

In order to verify the proposed method, we considered two artificial obstructions at different locations (Fig. 11 (a)) in the normal UA. The flow rate here is 15 L/min, which is same as that for the obstructed UA. Point C in the normal UA is too close to the branch of the nasal passages, and in order to avoid the influence of the branch, we created another point C′. Furthermore, based on information from our medical collaborators, point G is the least likely place for an anatomic obstruction, and points A and B (cf. Fig. 9) are in the nasal cavity whose obstruction is not considered. Thus, we added two spheres with different diameters to mimic the obstructions between points C′ and D, and between points E and F. The sphere diameter of the latter is larger than that of the former because the cross-sectional area in the region E-F is larger than that in the region C′–D. Since the pressure and its spatial derivatives are time-dependent, we performed time-averaging and presented the time-averaged values of the first derivative of pressure at four points C′, D, E and F in Fig. 11 (b). The negative sign in the plotted derivative $- \partial p/ \partial z$ in Fig. 11 (b) is because the main flow direction is in the opposite direction of the coordinate z during the inspiration. It is clear from Fig. 11 (b) that for the sphere between points C′ and D, the maximum change in the magnitude of the time-averaged $\partial p/ \partial z$ is between C′ and D. Similarly, for the sphere between points E and F, the maximum change in the magnitude of $\partial p/ \partial z$ occurs between E and F. This result proves that the maximum change in $\partial p/ \partial z$ occurs *in the region of the blockage* in the two artificially-obstructed UAs. However, in order to pinpoint the location of the narrowest section we need to plot the distribution of the time-averaged second derivative $\partial^2 p/ \partial z^2$ (cf. Fig. 10 (b)) as shown in red lines in Fig. 11 (b). It's clear that the maximum positive values of $\partial^2 p/ \partial z^2$ occur at point S1 (between C′ and D) and point S2 (between E and F).

We now examine whether the above finding is also true for the naturally-obstructed UA. The time-averaged $\partial p/ \partial z$ at the four points C, D, E and F in the obstructed UA is presented for both the inspiration and expiration in Fig. 12. Both Figs. 12 (a) and (b) show that the maximum change of the time-averaged $\partial p/ \partial z$ occurs between points D and E for both inspiration and expiration. However, in order to pinpoint the narrowest section we plot $\partial^2 p/ \partial z^2$ in the same figure. It is clear that point S4 is where $\partial^2 p/ \partial z^2$ attains its maximum positive values (associated with minimum pressure) for both inspiration and expiration. This location is consistent with the location of adenotonsillar hypertrophy. In other words, the obstruction location which we determined using the maximum positive value of $\partial^2 p/ \partial z^2$ is in excellent agreement with patient's CT scan. The method of maximum positive $\partial^2 p/ \partial z^2$ is now verified.

6.4. Discussion

It should be emphasized that it is not possible to locate the UA obstruction by examining the instantaneous 3D velocity or pressure fields since the flow contains zones with natural recirculation and vortical structures that are not caused by the obstruction. In contrast, the maximum positive $\partial^2 p/ \partial z^2$ uniquely identifies the obstruction.

Of course we knew in advance the locations of the artificial and real obstructions, but our objective was to develop a reliable method to locate obstructions in future cases for which there is no prior knowledge of the obstruction location. Also, our method is applicable to any kind of UA with obstruction, although here we only considered pediatric UA as an example.

7. Conclusions

In this study, we developed a DNS-LBM solver using both BGK and MRT collision operators. Several canonical flows, including the 2D laminar Poiseuille flow, 2D Taylor-Green vortex flow, 3D laminar curved pipe flow, 3D turbulent channel flow and 3D turbulent flow in an idealized UA, were used to validate the solver. Our DNS-LBM results agree with the analytical solutions, and with the experimental and numerical results.

The validated solver was then used to simulate the laminar-transitional-turbulent flow in a normal UA and an obstructed UA, which were reconstructed from CT scan data. Both inspiration and expiration flows for these two UAs were studied. Velocity and vorticity contours in several selected sections are presented and discussed. Recirculation flow, secondary flow and jet flow are found in the UA. Instantaneous velocity and pressure signals at different locations in the UAs were also investigated. The results show that the amplitude and frequency of pressure fluctuations are reduced in the obstructed UA. More importantly, we introduced a method for locating the UA obstruction in which the maximum change in the time-averaged first spatial derivative of pressure $\partial p/\partial z$ locates the *region* of the obstruction whereas the maximum positive value of the local time-averaged second derivative $\partial^2 p/\partial z^2$ *pinpoints* the blockage. We validated that method by comparing the result with a normal UA with two different artificial obstructions and a patient-specific obstructed UA.

References

Ball CG, Uddin M, Pollard A. Mean Flow Structures Inside the Human Upper Airway. Flow, Turbulence and Combustion. 2008; 81:155–188.

Bespalko D, Pollard A, Uddin M. Direct Numerical Simulation of Fully-Developed Turbulent Channel Flow Using the Lattice Boltzmann Method and Analysis of OpenMP Scalability. High Performance Computing Symposium. 2009:1–22.

Boyd J, Buick JM. Three-dimensional modelling of the human carotid artery using the lattice Boltzmann method: I. model and velocity analysis. Physics in Medicine and Biology. 2008; 53:5767–5779. [PubMed: 18824786]

Calay RK, Kurujareon J, Holdø AE. Numerical simulation of respiratory flow patterns within human lung. Respiratory physiology & neurobiology. 2002; 130:201–21. [PubMed: 12380010]

Choi J, Tawhai MH, Hoffman Ea, Lin CL. On intra- and intersubject variabilities of airflow in the human lungs. Physics of Fluids. 2009; 21:101901. [PubMed: 19901999]

Deng HB, Xu YQ, Chen DD, Dai H, Wu J, Tian FB. On numerical modeling of animal swimming and flight. Computational Mechanics. 2013; 52:1221–1242.

d'Humières D, Ginzburg I, Krafczyk M, Lallemand P, Luo LS. Lattice Boltzmann Multiple-relaxation-time models in three dimensions. Philosophical Transactions of the Royal Society of London, Series A. 2002; 360:427–451.

Doorly DJ, Taylor DJ, Schroter RC. Mechanics of airflow in the human nasal airways. Respiratory physiology & neurobiology. 2008; 163:100–110. [PubMed: 18786659]

Eitel G, Freitas R, Lintermann A, Meinke M, Schröder W. Numerical Simulation of Nasal Cavity Flow Based on a Lattice-Boltzmann Method Notes on Numerical Fluid Mechanics and Multidisciplinary. New Results in Numerical and Experimental Fluid Mechanics VII, Notes on Numerical Fluid Mechanics and Multidisciplinary Desig. 2010; 112:513–520.

Finck M, Hänel D, Wlokas I. Simulation of nasal flow by lattice Boltzmann methods. Computer in Biology and Medicine. 2007; 37:739–749.

Gambaruto AM, Taylor DJ, Doorly DJ. Decomposition and description of the nasal cavity form. Annals of biomedical engineering. 2012; 40:1142–1159. [PubMed: 22160578]

Guo Z, Zheng C, Shi B. An extrapolation method for boundary conditions in lattice Boltzmann method. Physics of Fluids. 2002; 14:2007–2010.

Han D, Ye J, Wang J, Yang Q, Lin Y. Determining the site of airway obstruction in obstructive sleep apnea with airway pressure measurements during sleep. The Laryngoscope. 2002; 112:2081–2085. [PubMed: 12439185]

Hörschler I, Schröder W, Meinke M. On the assumption of steadiness of nasal cavity flow. Journal of Biomechanics. 2010; 43:1081–1085. [PubMed: 20080240]

Hudgel D. Variable site of airway narrowing among obstructive sleep apnea patients. Journal of Applied Physiology. 1986; 61:1403–1409. [PubMed: 3781956]

Humphrey, JaC; Iacovides, H.; Launder, BE. Some numerical experiments on developing laminar flow in circular-sectioned bends. Journal of Fluid Mechanics. 1985; 154:357–375.

Johnstone A, Uddin M, Pollard A, Heenan A, Finlay WH. The flow inside an idealised form of the human extra-thoracic airway. Experiments in Fluids. 2004; 37:673–689.

Katsantonis GP, Moss K, Miyazaki S, Walsh J. Determining the site of airway collapse in obstructive sleep apnea with airway pressure monitoring. The Laryngoscope. 1993; 103:1126–1131. [PubMed: 8412449]

Kim J, Moin P, Moser R. Turbulence statistics in fully developed channel flow at low Reynolds number. Journal of Fluid Mechanics. 1987; 177:133–166.

Kim YH, Xu X, Lee JS. The effect of stent porosity and strut shape on saccular aneurysm and its numerical analysis with lattice Boltzmann method. Annals of biomedical engineering. 2010; 38:2274–2292. [PubMed: 20300847]

Kleinstreuer C, Zhang Z. Airflow and Particle Transport in the Human Respiratory System. Annual Review of Fluid Mechanics. 2010; 42:301–334.

Lin C, Tawhai M. Characteristics of the turbulent laryngeal jet and its effect on airflow in the human intra-thoracic airways. Respiratory physiology & neurobiology. 2007; 157:319–339.

Lintermann, A.; Meinke, M.; Schröder, W. Investigations of Nasal Cavity Flows based on a Lattice-Boltzmann Method. In: Resch, M.; Wang, X.; Bez, W.; Focht, E.; Kobayashi, H.; Roller, S., editors. High Performance Computing on Vector Systems 2011. Springer; Berlin/Heidelberg: 2012. p. 143-158.

Mihaescu M, Murugappan S, Kalra M, Khosla S, Gutmark E. Large Eddy Simulation and Reynolds-Averaged Navier-Stokes modeling of flow in a realistic pharyngeal airway model: an investigation of obstructive sleep apnea. Journal of Biomechanics. 2008; 41:2279–2288. [PubMed: 18514205]

Munn LL, Dupin MM. Blood cell interactions and segregation in flow. Annals of biomedical engineering. 2008; 36:534–544. [PubMed: 18188702]

Mylavarapu G, Murugappan S, Mihaescu M, Kalra M, Khosla S, Gutmark E. Validation of computational fluid dynamics methodology used for human upper airway flow simulations. Journal of Biomechanics. 2009; 42:1553–1559. [PubMed: 19501360]

Na Y, Chung KS, Chung SK, Kim SK. Effects of single-sided inferior turbinectomy on nasal function and airflow characteristics. Respiratory physiology & neurobiology. 2012; 180:289–297. [PubMed: 22227321]

Pollard A, Uddin M, Shinneeb A, Ball C. Recent advances and key challenges in investigations of the flow inside human oro-pharyngeal-laryngeal airway. International Journal of Computational Fluid Dynamics. 2012; 26:363–381.

Qian Y, D'Humières D, Lallemand P. Lattice BGK models for Navier-Stokes equation. Europhysics Letters. 1992; 17:479–484.

Skatvedt O. Continuous pressure measurements during sleep to localize obstructions in the upper airways in heavy snorers and patients with obstructive sleep apnea syndrome. European Archives of Otorhinolaryngology. 1995; 252:11–14. [PubMed: 7718222]

Succi, S. Lattice Boltzmann equation for fluid dynamics and beyond. Clarendon Press; Oxford: 2001.

Sukop, MC.; Thorne, DTJ. Lattice Boltzmann modeling: An introduction for geoscientists and engineers. Springer; Berlin: 2005.

Wen J, Inthavong K, Tu J, Wang S. Numerical simulations for detailed airflow dynamics in a human nasal cavity. Respiratory physiology & neurobiology. 2008; 161:125–135. [PubMed: 18378196]

Xi J, Berlinski A, Zhou Y, Greenberg B, Ou X. Breathing resistance and ultrafine particle deposition in nasal-laryngeal airways of a newborn, an infant, a child, and an adult. Annals of biomedical engineering. 2012; 40:2579–2595. [PubMed: 22660850]

Yoganathan A, He Z, Casey Jones S. Fluid mechanics of heart valves. Annual Review of Biomedical Engineering. 2004; 6:331–362.

Zhang Z, Kleinstreuer C. Laminar-to-turbulent fluid nanoparticle dynamics simulations: Model comparisons and nanoparticle-deposition applications. International Journal for Numerical Methods in Biomedical Engineering. 2011; 27:1930–1950.

Zhu JH, Lee HP, Lim KM, Lee SJ, Wang DY. Evaluation and comparison of nasal airway flow patterns among three subjects from Caucasian, Chinese and Indian ethnic groups using computational fluid dynamics simulation. Respiratory physiology & neurobiology. 2011; 175:62–69. [PubMed: 20854936]

Highlights

- We developed a lattice-Boltzmann method to predict the flow in the upper airway (UA).

- The time-averaged pressure gradient is used to locate the region of UA obstruction.

- The second derivative of pressure pinpoints the exact location of the UA obstruction.
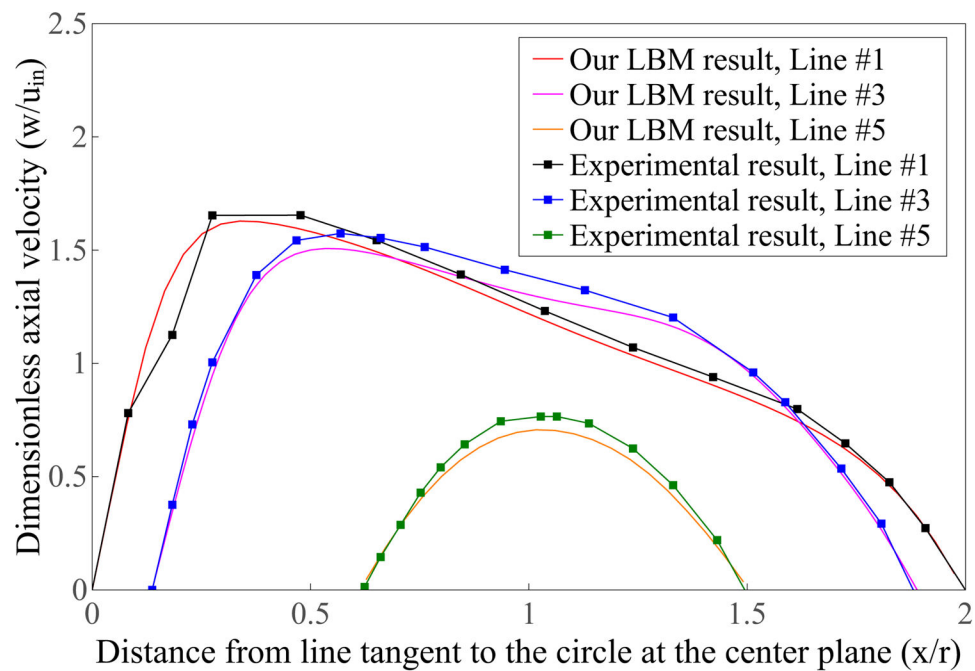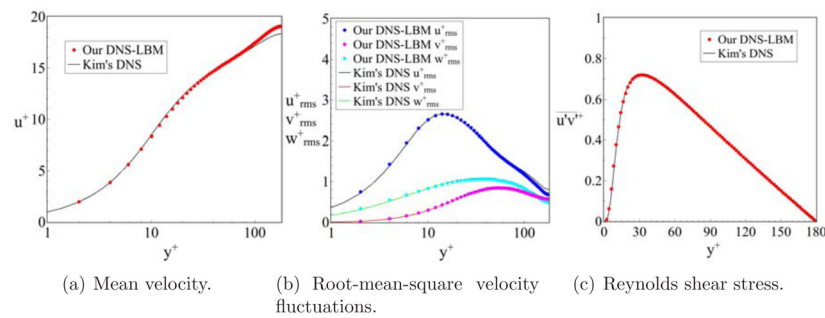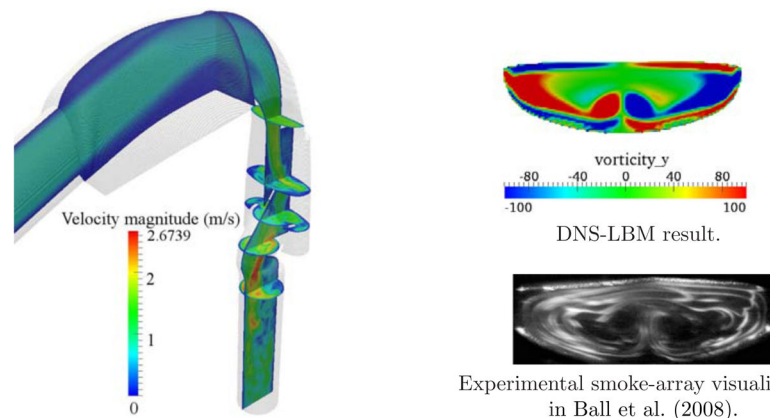
Wang and Elghobashi

Page 14

Figure 1.
Comparison between the present DNS and the experimental data of Humphrey et al. (1985) for the velocity profiles in a curved pipe.

Wang and Elghobashi

(a) Mean velocity. (b) Root-mean-square velocity fluctuations. (c) Reynolds shear stress.

Figure 2.

Results of the 3D turbulent channel flow with $Re_\tau = 180$. Comparison between the present DNS and DNS of Kim et al. (1987).

(a) Instantaneous velocity contours.

DNS-LBM result.

Experimental smoke-array visualization
in Ball et al. (2008).

(b) Instantaneous results in cross section
in the oropharynx.

Figure 3.
Results of the idealized UA model.
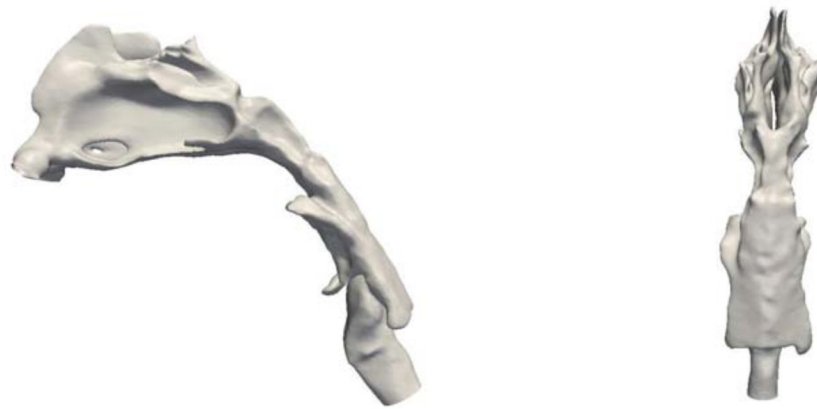
(a) Normal UA. Left: sagittal view; Right: dorsal view.

(b) Obstructed UA. Left: sagittal view; Right: dorsal view.

Figure 4.
Two patient-specific models of the UA used in the simulations.
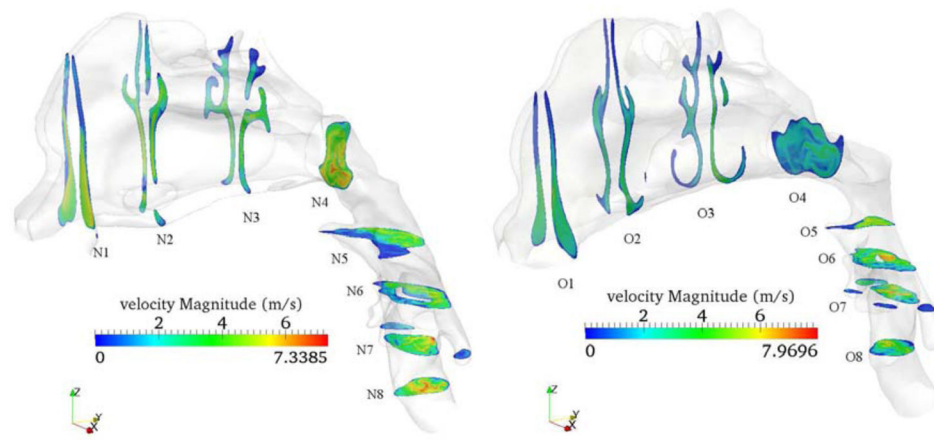
(a) Instantaneous velocity contours at cross sections. Left: normal UA; Right: obstructed UA.
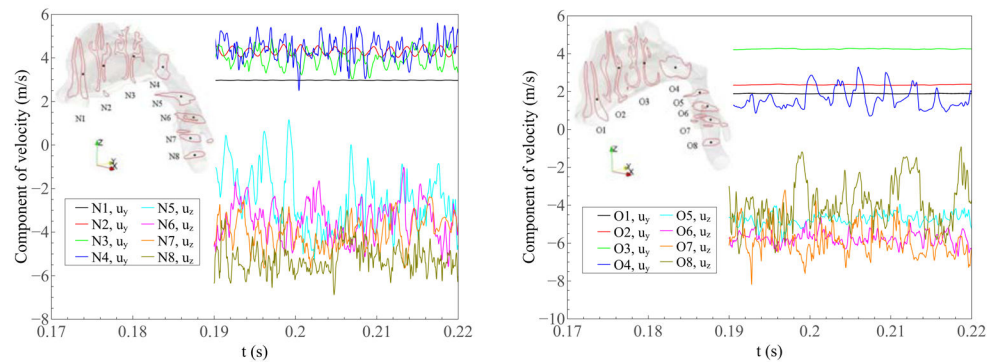
(b) Temporal variations of velocity components at points in the cross sections. Left: normal UA; Right: obstructed UA.

Figure 5.
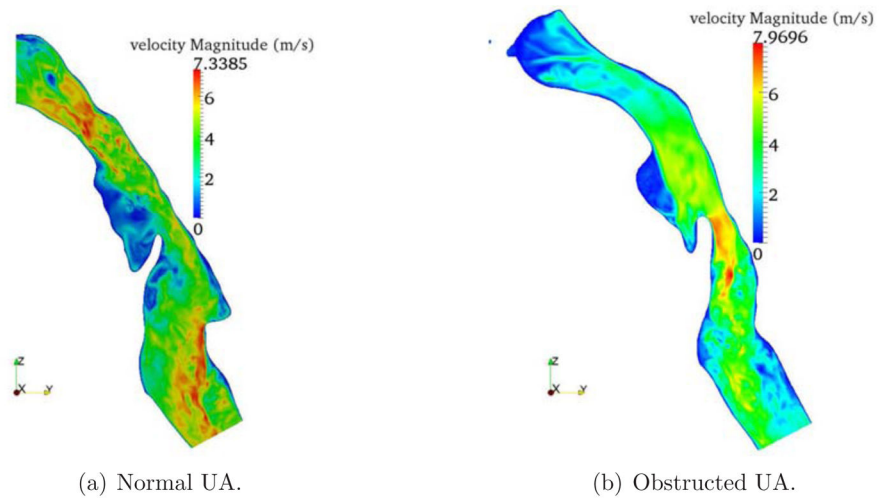Instantaneous velocity contours and temporal variations of velocity components during inspiration.

(a) Normal UA.   (b) Obstructed UA.
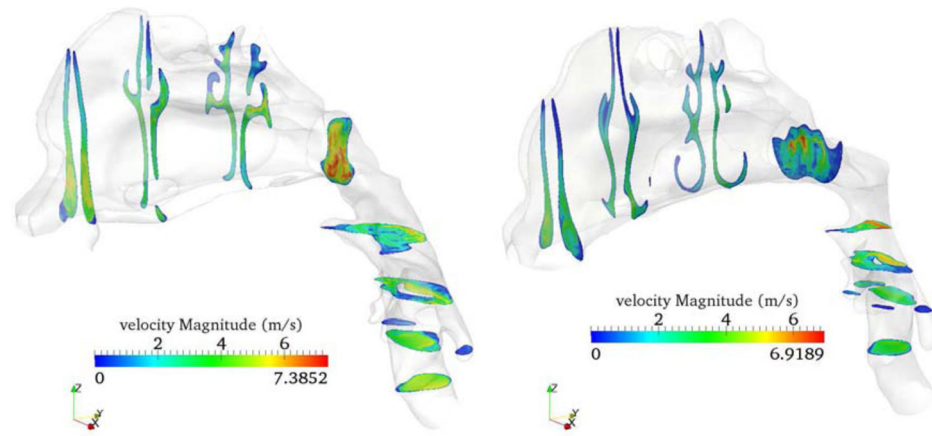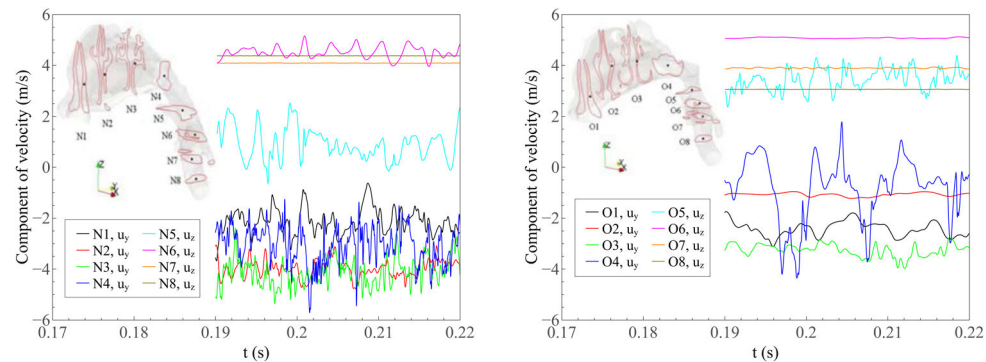
Figure 6.
Instantaneous velocity contours in the sagittal plane during inspiration.

(a) Instantaneous velocity contours at cross sections. Left: normal UA; Right: obstructed UA.

(b) Temporal variations of velocity components at points in the cross sections. Left: normal UA; Right: obstructed UA.

Figure 7.
Instantaneous velocity contours and temporal variations of velocity components during expiration.
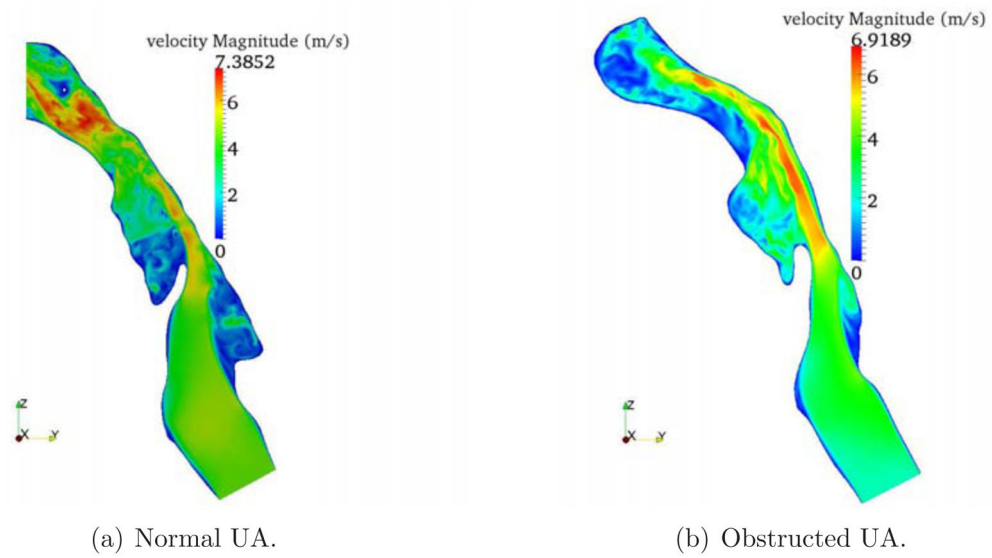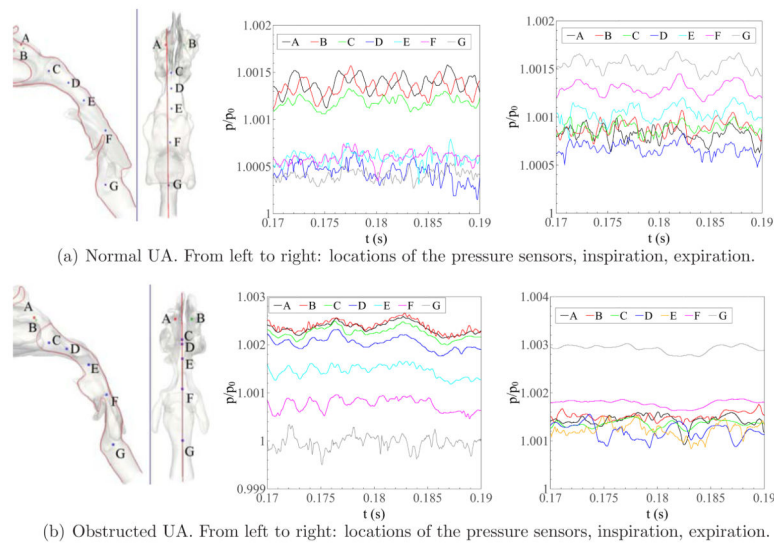
(a) Normal UA.

(b) Obstructed UA.

Figure 8.
Instantaneous velocity contours in the sagittal plane during expiration.

(a) Normal UA. From left to right: locations of the pressure sensors, inspiration, expiration.

(b) Obstructed UA. From left to right: locations of the pressure sensors, inspiration, expiration.

Figure 9.
Temporal variations of pressure at seven points (A–G) in the normal and obstructed UAs.

(a) Sketch and pressure distribution.
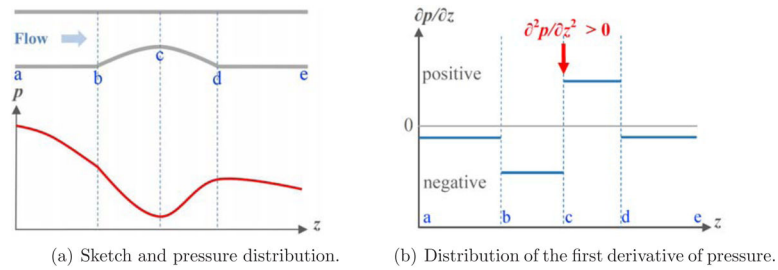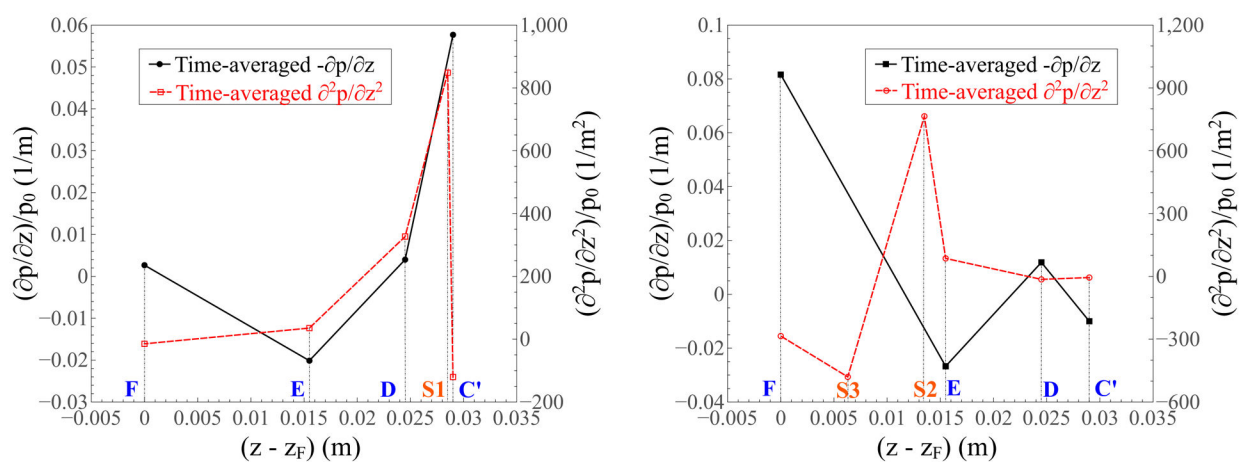
(b) Distribution of the first derivative of pressure.

Figure 10.
Flow past an obstruction in a channel.

(a) Locations of the artificial obstructions in the normal UA. Left: obstruction between points C′ and D; Right: obstruction between points E and F.

(b) Time-averaged first and second derivatives of pressure at four points in the normal UA. Left: obstruction between points C′ and D; Right: obstruction between points E and F.

Figure 11.

Artificial obstructions in the normal UA and time-averaged first and second derivatives of pressure during inspiration.

Wang and Elghobashi

Page 25
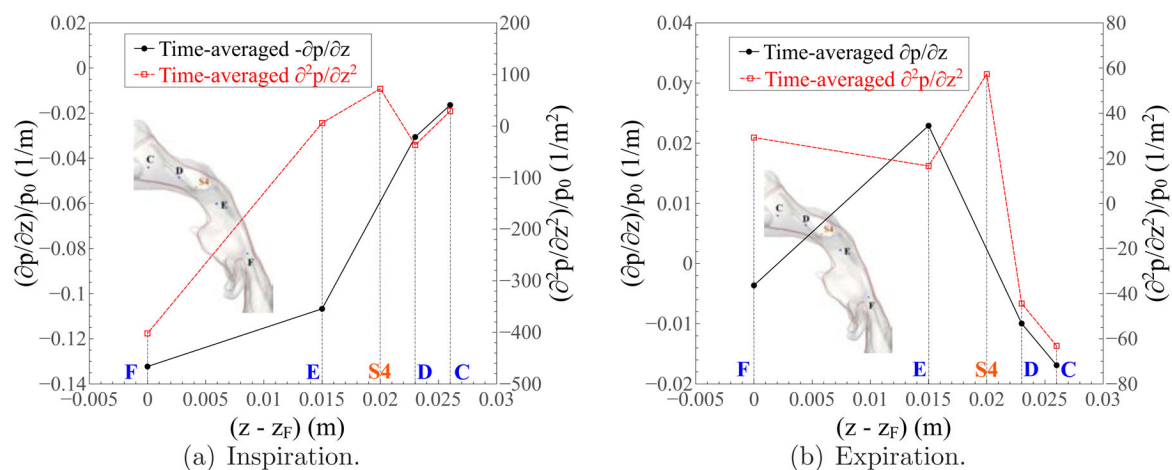
Figure 12.
Time-averaged first and second derivatives of pressure at four points in the naturally-obstructed UA.

Table 1

CT scan parameters.

Case	Scan resolution (mm)	Scan thickness (mm)	Segmentation criteria
Normal UA	$0.438 \times 0.438 \times 0.3$	0.6	[−1024, −350]
Obstructed UA	$0.367 \times 0.367 \times 0.7$	1.5	[−1024, −350]

Table 2

Parameters used in the simulations of UAs.

Case	Flow rate (L/min)	$|U_{inl}|$ (m/s)	Mesh size (million nodes)	δx (10^{-5}m)	δt (10^{-7}s)	Processor hours on BW
Normal UA Inspiration	25	3.00	159	5.46	2.25	250,000
Normal UA Expiration	25	4.43	208	4.99	1.88	300,000
Obstructed UA Inspiration	15	2.00	30	8.92	5.45	25,000
Obstructed UA Expiration	15	2.23	40	8.10	4.95	35,000